International Journal of Heat and Mass Transfer 51 (2008) 5721–5731

Contents lists available at ScienceDirect

International Journal of Heat and Mass Transfer

journal homepage: www.elsevier.com/locate/ijhmt

Vapor/liquid phase interaction in flare flashing sprays used in dermatologic cooling

H. Vu [a], O. García-Valladares [b], G. Aguilar [a,*]

[a] Department of Mechanical Engineering, University of California, Riverside, CA 92521, USA
[b] Centro de Investigación en Energía, Universidad Nacional Autónoma de México, Privada Xochicalco S/N, 62580 Temixco, Morelos, México

ARTICLE INFO

Article history:
Received 30 October 2007
Received in revised form 4 April 2008
Available online 9 June 2008

Keywords:
Cryogen spray cooling
Port wine stain
Dermatologic laser surgery

ABSTRACT

Little knowledge exists concerning the atomization mechanisms and dispersion of flashing sprays in dermatologic cooling. This study examines flashing of a high superheat fluid flowing through micro tube nozzles resembling current medical devices. A one-dimensional, semi-empirical model of refrigerant flow through capillary tubes is used to quantify internal flow characteristics. These results provide nozzle exit conditions that are then correlated to external spray characteristics determined experimentally. One-dimensional expressions for external vapor/liquid interaction are developed to determine evolution of droplet size distribution and explain measured droplet accelerations near the nozzle exit. Droplet drag coefficients are subsequently calculated and compared to existing literature.

1. Introduction

In dermatologic laser surgeries of vascular lesions, particularly port wine stains, precooling of the epidermis by means of a refrigerant cooling spray reduces the likelihood of superficial thermal damage due to laser heating [1,2]. Saturated liquid refrigerant is released to the atmosphere by a throttling process through a narrow tube orifice. Because of the superheated condition of the refrigerant following sudden depressurization, homogeneous vapor nucleation and explosive boiling breakup of the liquid occurs. This mechanism of spray atomization is known as *flashing*. Following atomization, the remaining liquid droplets impinge on the targeted skin surface, resulting in intense, short-duration cooling. This method of skin cooling has been used in conjunction with laser therapy for over a decade. However, clinical studies have demonstrated that the success rate of these treatments remains as low as 25%. Insufficient cooling, and non-uniformities in cooling protection [3] may be significant reasons for this therapeutic outcome. Substantial work has already been performed on the optical [4,5] and spray cooling heat transfer aspects of the problem [6–9] but little attention has been given to the spray atomization mechanisms. This, coupled with the current poor fundamental understanding of flashing atomization mechanisms, in general, are the motivations for the current work. It is through this knowledge that spray systems can be modified to improve control of spray characteristics and the resulting cooling protection.

Flash atomizing sprays have been studied since the early 1960s with Brown and York [10] being one of the first to observe and document the phenomenon. Since then, several other works have furthered our understanding of flashing phenomena. Reitz [11] and Park and Lee [12] performed visualization studies in which spray characteristics were correlated to varying degrees of superheat and nozzle characteristics. Reitz [11] observed the effects of nozzle exit surface roughness on the resulting spray. Park and Lee [12] developed qualitative relations between internal flow characteristics and the resulting sprays by visualization using a novel transparent nozzle. Generally, it was found by both works that increasing superheat improved jet atomization. Peter et al. [13] identified four spray breakup regimes: non-shattering, partially shattering, stagewise shattering, and flare flashing. They measured temperature evolution characteristics of each type of spray. Later, Allen [14,15] performed a comprehensive quantitative study of spray droplet velocity and diameter distributions of flashing propane sprays. Attempts to model flashing sprays have also been carried out by Sher and Elata [16] and Zeng and Lee [17].

Besides dermatologic spray cooling, current interest in flashing sprays continues as a result of attempts to better understand accidental industrial releases of pressurized liquids [18,19] and increase atomization of fuel injection sprays in the automotive industry [20–22].

In this work, a one-dimensional model of refrigerant flow in capillary tube expansion devices [23–25] is used to characterize internal flashing nozzle flow. The model is validated for this present case, and combined with detailed external spray studies, provides new insight into this atomization process. No known work has attempted to quantitatively characterize the internal flow conditions within the nozzle and relate them to quantitative external spray characteristics. The present study examines the case of flare flashing of a high superheat liquid in large L/D ratio nozzles, a situation similar to current dermatologic cooling spray systems.

* Corresponding author. Tel.: +1 951 827 7717; fax: +1 951 827 2899.
E-mail address: gaguilar@engr.ucr.edu (G. Aguilar).

0017-9310/$ - see front matter © 2008 Elsevier Ltd. All rights reserved.
doi:10.1016/j.ijheatmasstransfer.2008.04.020

Nomenclature

A	cross section area [m^2]
$\vec{A}$	droplet surface area vector [m^2]
C	heat capacity [J kg^{-1} K^{-1}]
C_D	drag coefficient
C_S	control surface
C_V	control volume
d	droplet diameter [m]
$\bar{d}$	mean droplet diameter [m]
D	nozzle diameter [m]
D_{10}	arithmetic average droplet diameter [m]
f	friction factor
F_d	drag force [N]
g	gravity [m s^{-2}]
G	vapor phase generation [kg]
h	enthalpy [J kg^{-1}]
h_{fg}	latent heat of vaporization [J kg^{-1}]
k	Gaussian distribution function
L	length [m]
m	total mass ($m_l + m_g$) [kg]
$\dot{m}$	total mass flow rate ($\dot{m}_g + \dot{m}_l$) [kg s^{-1}]
p	pressure [Pa]
P	perimeter [m]
$\dot{q}$	heat flux per unit area [W m^{-2}]
r	radius [m]
R_{134a}	gas constant for R134a [J kg^{-1} K^{-1}]
s	specific entropy [J kg^{-1} K^{-1}]
t	time [s]
T	temperature [K]
u	internal energy [J kg^{-1}]
v	velocity [m s^{-1}]
V	droplet volume [m^3]
$\vec{V}$	droplet evaporation velocity vector [m s^{-1}]
$\forall$	total droplet volume [m^3]
x_g	mass fraction (vapor quality)
z	axial coordinate

Greek symbols

α	heat transfer coefficient [W m^{-2} K^{-1}]
Δz	spatial discretization step [m]
ε_g	void fraction
ϕ	generic dependent variable
Φ	two-phase frictional multiplier
θ	inclination angle [rad]
ρ	density [kg m^{-3}]
σ	standard deviation
τ	shear stress [N m^{-2}]
ξ	Eq. (3) ($h + v^2/2 + gz\sin\theta$) [J kg^{-1}]

Subscripts

d	droplet
dis	discharge
f	fluid
g	gas or vapor
j	measurement location index within external spray
l	liquid
P	PDPA measurement probe
stag	stagnation
w	wall

Superscripts

$-$	arithmetical average over a C_V: $\bar{\phi} = (\phi_i + \phi_{i+1})/2$
$\sim$	integral average over a C_V: $\tilde{\phi} = (1/\Delta z)\int_z^{z+\Delta z}\phi dz$
$*$	value at previous iteration

$[X]_i^{i+1} = X_{i+1} - X_i$

2. Experimental methods

2.1. Spray system

The spray fluid used is refrigerant R134a (tetrafluoroethane) which is kept at a saturation pressure of ~600 kPa in a pressurized container. The liquid is connected to a miniature solenoid valve (099-0169-900, Parker-Hannifin, Fairfield, NJ) via a high pressure hose. At the exit of the valve is a plain-orifice stainless steel tube nozzle of 0.5 mm inner diameter. Three different tube lengths of 20, 40 and 80 mm are used corresponding to L/D ratios of 40, 80, and 160, respectively. The spray system is oriented vertically, with the flow exiting downward.

2.2. Capillary tube flow model

2.2.1. Mathematical formulation

In this section the mathematical formulation of two-phase flow inside a characteristic control volume (C_V) of a nozzle is presented. The C_V is shown schematically in Fig. 1a, where 'i' and '$i+1$' represent the inlet and outlet mass flow cross section areas, respectively.

Taking into account the physical characteristics of the nozzle (diameter, length, roughness, inclination angle, etc.), the governing equations have been integrated with the following assumptions: one-dimensional flow, constant internal diameter, uniform surface roughness, separated flow in which the liquid and gas velocities are treated independently, negligible axial heat conduction inside the fluid, negligible radiation effects and C_V of fixed dimensions. The general semi-integrated governing equations over the above mentioned finite C_V, have the following form:

Continuity:

$$[\dot{m}_g + \dot{m}_l]_i^{i+1} + \frac{\partial(m_g + m_l)}{\partial t} = 0 \tag{1}$$

Momentum:

$$[\dot{m}_g v_g]_i^{i+1} + [\dot{m}_l v_l]_i^{i+1} + \Delta z\frac{\partial(\tilde{\dot{m}}_g + \tilde{\dot{m}}_l)}{\partial t} = -[p]_i^{i+1}A - \tilde{\tau}_w P\Delta z - mg\sin\theta \tag{2}$$

Energy:

$$[\dot{m}_l\xi_l + \dot{m}_g\xi_g]_i^{i+1} + \frac{\partial(\bar{m}_l\bar{\xi}_l + \bar{m}_g\bar{\xi}_g)}{\partial t} - A\Delta z\frac{\partial\tilde{p}}{\partial t} = \tilde{\dot{q}}_w P\Delta z \tag{3}$$

where $\xi = h + v^2/2 + gz\sin\theta$.

Entropy:

$$[\dot{m}_l s_l + \dot{m}_g s_g]_i^{i+1} + \frac{\partial(\bar{m}_l\bar{s}_l + \bar{m}_g\bar{s}_g)}{\partial t} - \frac{\tilde{\dot{q}}_w P\Delta z}{\bar{T}_w} \geqslant 0 \tag{4}$$

The evaluation of the shear stresses is carried out by means of a friction factor f and a two-phase multiplier Φ which are included in the following expression for wall shear stress: $\tau_w = \Phi(f/4)(\dot{m}^2/2\rho A^2)$. The one-dimensional model also requires knowledge of the two-phase flow structure, which is evaluated by means of the void fraction ε_g as determined by empirical correlations (see below). The heat transfer through the nozzle wall and the fluid temperature are related by the convective heat transfer coefficient α, which is defined as: $\alpha = \dot{q}_w/(T_w - T_f)$.

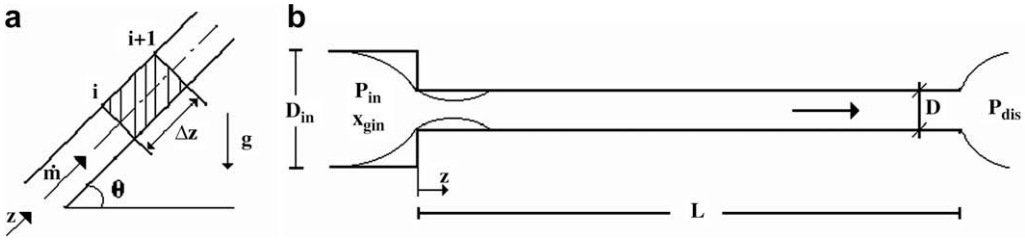

Fig. 1. (a) Flow inside a C_V and (b) schematic diagram of a nozzle.

Temperature, mass fraction and all the thermo-physical properties are calculated using matrix functions of the pressure and enthalpy obtained with REFPROP v7.0 [26]. Boundary conditions are specified at the inlet and outlet sections of the nozzle (Fig. 1b) and along the tube wall (wall surface roughness and heat flux or temperature distribution). At the *inlet section* the refrigerant is saturated so the appropriate inlet pressure (p_{in}) and vapor mass fraction (x_{gin}) are available. The *outlet* or *discharge section* pressure (p_{dis}) is either the critical pressure (to be determined) or atmospheric pressure, whichever is higher.

2.2.2. Evaluation of empirical coefficients

The mathematical model requires some additional local information generally obtained from empirical or semi-empirical correlations. After comparing different correlations presented in the technical literature, the following have been selected:

The void fraction (ε_g) is computed by a semi-empirical equation proposed by Rouhani and Axelsson [27] for a drift flux model that considers the effects of the mass velocity, surface tension and buoyancy. The friction factor (f) is evaluated from the expressions proposed by Churchill [28] with a correction factor (Φ) according to Friedel [29]. These correlations have been widely used in refrigeration system studies in the past.

The convective heat transfer coefficient (α) is evaluated using the Shah correlation [30] and natural convection between the nozzle tube and the ambient is considered using the correlation developed by Churchill and Chu [31]. However, our comparisons between numerical results considering heat transfer with the ambient air and adiabatic flow have shown that the difference between both simulations is small.

The simulation computes the mass flow rate of each phase at any location within the nozzle together with the flow variables (pressure, temperature, mass fraction, velocity, etc.).

2.2.3. Numerical resolution and algorithm

Because of the high gradients in flow variables present at the end of the nozzle, a non-uniform grid concentrated at the outlet section is generated as described in García-Valladares [32]. Mesh-independent solutions are obtained with each computational domain consisting of 300 C_V. For each C_V, a set of algebraic equations is obtained by the discretization of the governing Eqs. (1)–(4) [32]. The discretized equations are coupled using a fully-implicit, step-by-step method in the flow direction. From the known values at the inlet section and the wall boundary conditions, the variable values at the outlet of each C_V are iteratively obtained from the discretized equations. This solution (outlet values) is the inlet condition for the next C_V. A strict convergence condition, $(1 - |(\phi^*_{i+1} - \phi_i)/(\phi_{i+1} - \phi_i)|) < 10^{-7}$, must be verified in each C_V for passing to the next time step.

The numerical global algorithm is as follows: the inlet mass flow rate is iteratively estimated by means of a numerical Newton–Raphson algorithm to obtain critical or choked flow conditions. Critical flux conditions are reached when Eq. (4) is not verified in the last C_V, since entropy reaches its maximum value at the location of choking. To check critical conditions the criterion $dp/dz \to \infty$ is sometimes reported in the literature. For the cases presented here both criteria are equivalent.

After critical conditions are evaluated, the critical pressure and atmospheric pressure are compared. If the critical pressure is greater than atmospheric, the flow is critical and all calculated flow parameters remain valid. Otherwise, the flow is non-critical and the mass flow rate that offers an outlet pressure equal to atmospheric is evaluated by means of another Newton–Raphson algorithm.

2.3. Spray characterization

2.3.1. Droplet velocity and diameter

External spray droplet characteristics are determined using a Phase Doppler Particle Analyzer (PDPA; TSI Incorporated, Shoreview, MN) to measure the velocities and diameters of spherical droplets. A 300 mW Argon-Ion laser is used, producing beams of wavelength 488 nm and 514.5 nm and enabling velocity measurements in two axes. This study only considers axial velocities with respect to the nozzle, so only the 514.5 nm light beams are used. Because of the high density of the spray near the nozzle exit, the likelihood for beam extinction or the detection of multiple particles simultaneously in the measurement volume increases. Since the PDPA is essentially a single particle counter, these effects lead to a lower validated data rate. However, a lowered data rate does not necessarily impact the accuracy of the validated data since the rejected data is not biased toward a particular velocity or diameter range [33,34]. To compensate for the lowered data rate, more measurement runs are performed. Acquisition times for each run are kept below two seconds after the valve opens to prevent excessive cooling of the nozzle wall, which may influence spray formation. Within the temperature range of the current study (from −60 to 25 °C), refractive index changes for the liquid and gas phases are estimated to be less than 0.001, which is below the relevant precision level of the measurement system. Therefore, beam steering effects and sizing errors due to temperature gradients are assumed to be small. Yildiz et al. [35] and Allen and Bettis [36] have verified the ability to use laser Doppler techniques in the harsh optical environments of flashing sprays. More details on PDPA operation can be found elsewhere [33,34,37].

In order to reduce the influence of ambient air humidity on the measured spray characteristics, the solenoid valve and nozzle are contained within a custom-made clear acrylic chamber shown in Fig. 2a. Chamber walls are 12.7 mm (0.5 in) thick, and oriented to be perpendicular to the transmitting and receiving probes to minimize refractive effects. The chamber is flushed with dry air between measurement runs and relative humidity is maintained between 15% and 20%. The air temperature is kept between 22.5 and 24.5 °C and pressure is atmospheric (~100 kPa). The laser beam attenuation and refraction induced by the chamber walls significantly reduce the data rate of the horizontal velocity measurements, but this value is not used in the study.

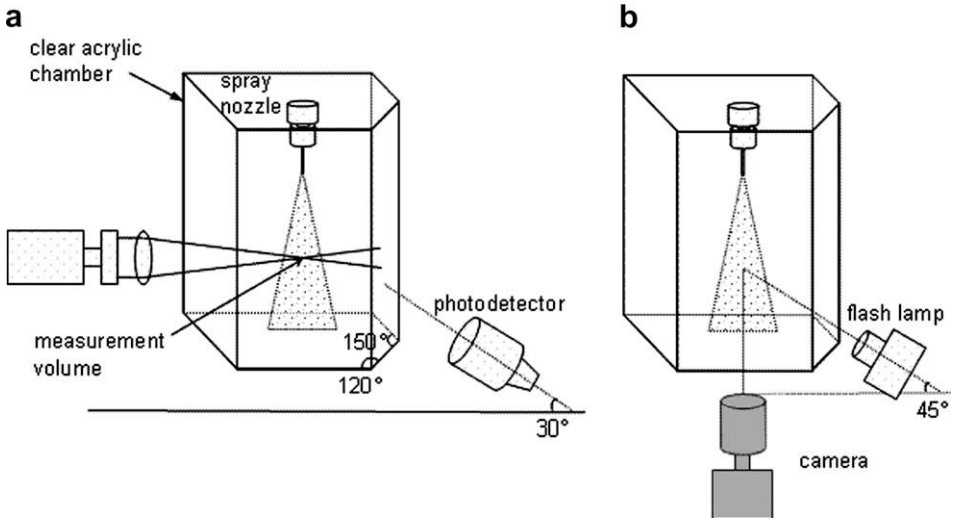

Fig. 2. Experimental spray characterization using (a) PDPA for droplet size and velocity and (b) flash lamp photography.

2.3.2. Mass flow rate

In order to validate the numerical model for the present study, mass flows are measured experimentally by weight. A small 12 oz can of R134a is attached to the spray assembly and everything is weighed before and after a five second spurt. This process is repeated five times for each nozzle length and the mass changes are averaged to determine mass flow rates. Errors in mass flow due to the weighing scale or solenoid valve response times are estimated to be less than ±0.1 g/s.

2.3.3. Temperature measurements

Spray temperature measurements are made by inserting a small (gage 36), fast-response type-K thermocouple (5TC-KK-K-36-36, Omega Engineering, Stamford, CT), supported by a rigid wood stick, into the spray centerline. The stick is oriented below the thermocouple and parallel to the spray axis to minimize its effect on flow conditions, and only makes contact with the thermocouple wire insulation. At the low humidity range used, ice formation was not observed on the thermocouple bead throughout the duration of the spray. Temperature measurements are also used to validate the internal flow model by comparing measurements to predicted values at the nozzle outlet. Errors in thermocouple measurements are estimated to be less than ± 1 °C for this thermocouple type and for the range of measurements taken.

2.3.4. Imaging

Imaging of the spray is carried out using a high-speed camera (Fastcam, Photron USA, San Diego, CA). A 20-W high-intensity xenon arc flash lamp (FYD-1150-B Litepac, Perkin Elmer, Salem, MA) with a 5-μs flash duration is used to illuminate and "freeze" the spray for imaging, for qualitative analysis, and for tracking spray cone expansion. The flash is oriented at approximately 45 degrees with respect to the camera as shown in Fig. 2b.

2.3.5. Gas velocity measurement

In order to determine the gas phase velocity of the external flow, a Pitot-type technique is employed using a diaphragm-based pressure transducer (PX302-200 GV, Omega Engineering, Stamford, CT). A short length of narrow tubing is attached to the end of the transducer in order to localize the area of measurement to the central axis of the spray and extend it away from the large transducer body (Fig. 3). The opening of the tube is inserted into the spray axis perpendicular to the flow to measure the stagnation

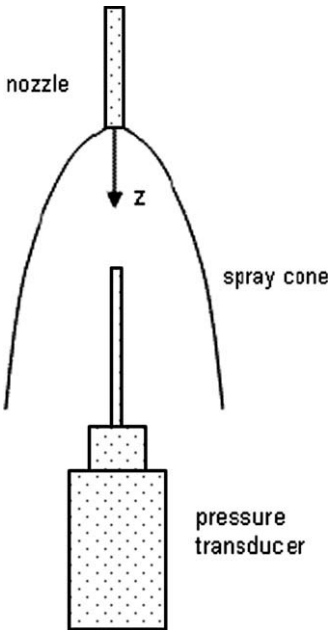

Fig. 3. Schematic of spray stagnation pressure measurement.

pressure, p_{stag}. Steady-state pressure measurements are used to determine the velocity of the gas flow from Eqs. (5a) and (5b):

$$p_{meas} = p_{stag} - p_{static} = \rho_g \frac{v^2}{2} \tag{5a}$$

$$v = \sqrt{2\frac{p_{stag} - p_{static}}{\rho_g}} \tag{5b}$$

Because the transducer measures gage pressure, the static pressure, p_{static}, is the pressure within the spray that is above ambient. By orienting the pressure transducer perpendicular to the flow direction, p_{static} could be measured and was found to be equal to the surrounding ambient pressure for all spray locations, $z > 0$ mm. The density of the gas phase, ρ_g, is dependent on temperature and mass fraction of R134a vapor. These values are computed from measurable quantities and will be described in Section 3.4. Based on the accuracy of the pressure transducer, estimated errors in calculated velocities are expected to be within ±35 m/s. For a measured

velocity range of nearly 0–300 m/s, this represents a sizable error so results should be interpreted accordingly. On the other hand, the influence of the impact of the liquid droplets on the pressure reading was found to be insignificant. Details for this assertion are given in the Appendix.

3. Results and discussion

3.1. Model validation

Results for the numerical model validation are given in Table 1. The three analyzed cases present choked (critical) flow. The mass flow rate and exit temperatures calculated for all of them are within reasonable errors to experimental values (see Table 1). The numerical model is, thus, capable of predicting the appropriate mass flow rates and exit flow temperatures. Because the model has been validated extensively for refrigeration applications, the other predicted flow variables of interest are taken to be accurate.

3.2. Internal flow

Fig. 4 presents internal nozzle flow data for variables of interest. Fig. 4a indicates that both pressure and temperature are reduced continuously along the length of the tube nozzle. Lengthening the nozzle offers more wall surface area and higher frictional resistance so the pressure is reduced further. Temperature reductions are due to the latent heat of vaporization and expansion of the gas phase. Hence, exit values of pressure and temperature for longer nozzles are lower due to the increased wall effects.

Fig. 4b shows that liquid velocity increases gradually along the length of the nozzle though slightly lower liquid exit velocities are apparent for longer nozzles. This corroborates the reduced mass flow rates shown earlier in Table 1 and is likely due to the greater frictional resistance. Higher gas phase velocities are observed, however, for the longer nozzles. Longer nozzles, therefore, have larger exit velocity differentials between phases.

Fig. 4c shows both mass (x_g) and void (ε_g) fractions of the gas phase. Again, the liquid evaporates as it progresses through the nozzle due to the pressure drop. Longer nozzles produce a slight increase in the outlet vapor quality (mass fraction) and void fraction (volume fraction of vapor).

3.3. External flow

Centerline spray characteristics of the external flow are given in Fig. 5. Remarkably, the droplet velocities of Fig. 5a continue to dis-

Table 1
Model validation

	Experimental data		Numerical model			
Nozzle length [mm]	Mass flow [g/s]	Outlet temp. [K]	Mass flow [g/s]	Error [g/s]	Outlet temp. [K]	Error [K]
20	1.25	271.3	1.32	0.07	271.83	0.53
40	1.12	267.7	1.13	0.01	267.74	0.04
80	0.90	262.25	0.91	0.01	262.99	0.74

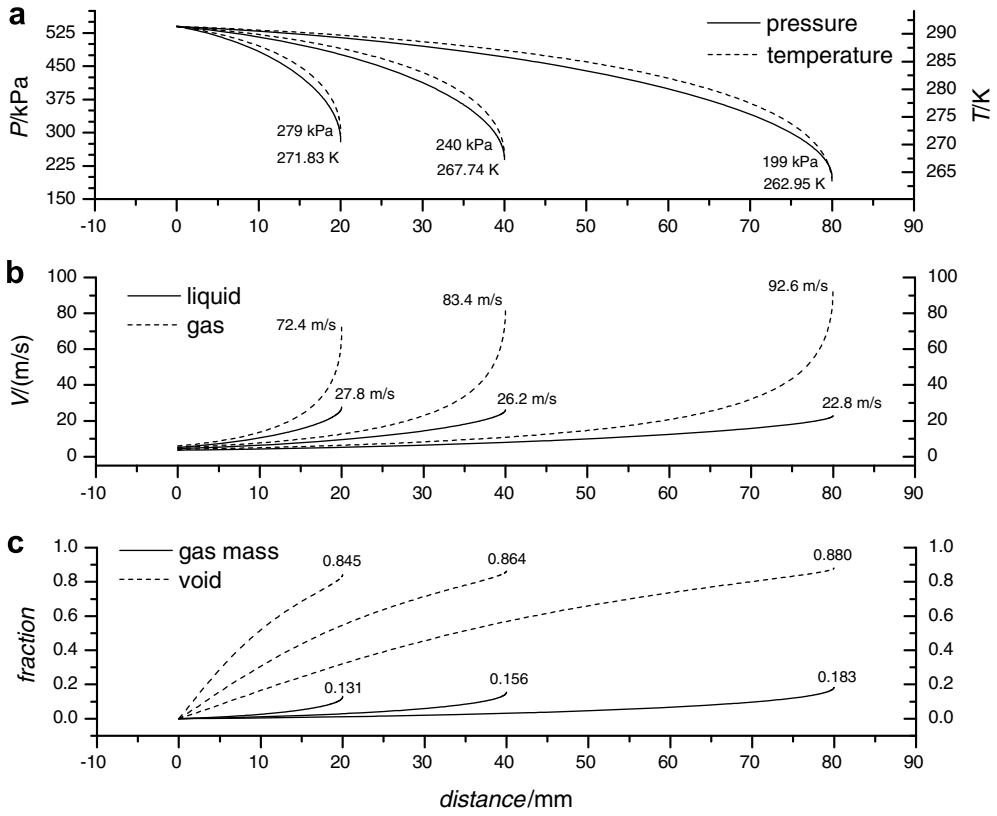

Fig. 4. Model results for internal nozzle (a) pressure and temperature, (b) velocity and (c) void fraction and mass fraction of gas. Exit values for each nozzle are indicated in the graphs.

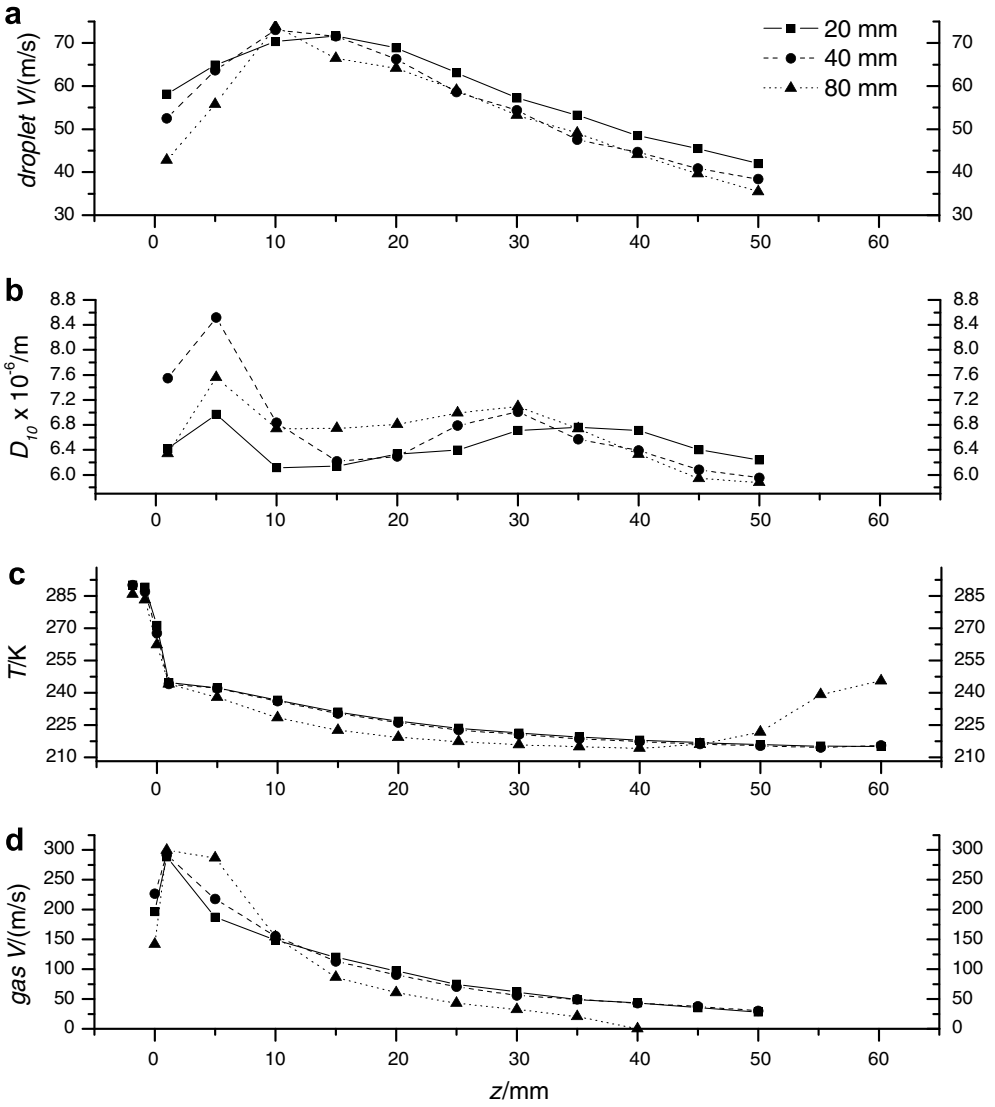

Fig. 5. Experimental results for spray characteristics: (a) droplet velocity, (b) arithmetic average droplet diameter, (c) spray temperature (d) gas velocity.

play an increase in magnitude away from the nozzle for a significant distance before decreasing again. This observation has also been made by Yildiz et al. [35] for similar sprays. The magnitude of acceleration of the spray in the near field of the nozzle appears to be larger for longer length nozzles, since they have lower exit velocities, yet achieve approximately the same maximum velocities. This may be due to the higher velocity differentials between the liquid and gas phases, as pointed out earlier. Once maximum velocities have been reached, droplet deceleration occurs at approximately the same rate for all nozzle lengths for $z > 25$ mm.

Measured arithmetic average droplet diameters (D_{10}) of Fig. 5b appear to be unstable within the range of 1–30 mm from the nozzle exit. Detectable droplet sizes appear to achieve maximum at 5 mm followed by an abrupt decrease. A slight increase occurs over the range of 15–30 mm, after which a consistent gradual decline ensues. The fluctuation in droplet sizes at $z < 30$ mm may be due to the low validation rate and low number of samples so D_{10} values may have large errors within this range [38], as mentioned before.

Spray temperatures are provided for all nozzle lengths in Fig. 5c. Some measurements are taken at 1 and 2 mm *within* the nozzle by insertion of the miniature thermocouple bead into the nozzle to demonstrate the abrupt temperature change near the nozzle exit. Temperatures decrease rapidly to approximately boiling temperature (~-26 °C) as the liquid flash boils upon exiting the nozzle. Spray temperatures continue to decrease beyond the boiling point, albeit at a much slower rate. This phenomenon was observed by Aguilar et al. [39] for R134a sprays and may be attributed to the low surface tension and latent heat of vaporization of the liquid (both about 1 order of magnitude lower than water), making continuous evaporation and cooling of the droplets possible. Temperatures for the 40 mm nozzle are very slightly lower than for 20 mm. Temperatures for the 80 mm nozzle are more significantly lower between the range of 1–40 mm. This could possibly be attributed to smaller or fewer droplets exiting the nozzle, which would reduce in temperature more easily. The increase in temperature occurring beyond 40 mm may be due to the complete evaporation of a significant number of droplets.

From spray pressure measurements, gas phase velocities are computed using Eq. (5b) and given in Fig. 5d. The determination of gas phase densities necessary for the calculations is explained in Section 3.4.2. Gas velocities accelerate to nearly 300 m/s for all nozzles before gradually decelerating, but remain higher than droplet velocities within about 20 mm from the nozzle exit. Afterwards, both phases are about the same. Gas velocities remain higher for the longer length nozzles up until about 10 mm, after which a more rapid deceleration occurs.

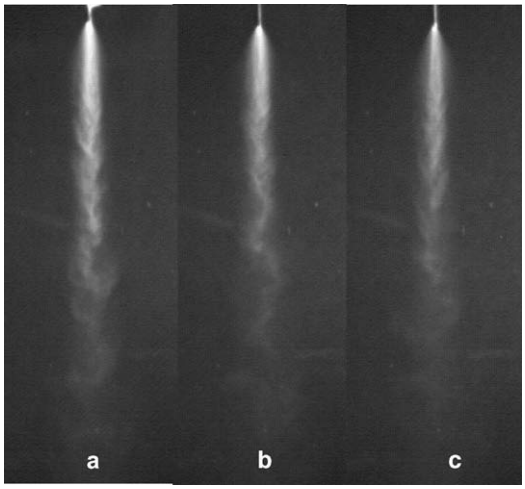

Fig. 6. Flash lamp photography images of the spray formed from a (a) 20 mm, (b) 40 mm, and (c) 80 mm nozzle.

Flash lamp photography images of the spray in Fig. 6 indicate visually the effect of nozzle length on the spray characteristics. With identical lighting conditions, there is a slight reduction in the intensity of the reflected flash light with increasing nozzle length. This may be due to the reduced flux of liquid at the nozzle exit, meaning fewer or smaller spray droplets. Spray penetration is also reduced indicating, again, that spray droplets will evaporate more quickly for longer length nozzles. Aside, from these observations, there appears to be little difference among the nozzle lengths. For all three cases, spray cone expansion seems to be very high within the first few mm from the nozzle, after which a more gradual expansion ensues.

3.4. Spray liquid/vapor interactions

A new treatment of the external spray is proposed, based on the exit flow parameters predicted by the internal flow model which provide all necessary boundary conditions at $z = 0$. This treatment explains the measured increase in spray droplet velocity away from the nozzle and is described below.

Because of the large void fraction and difference in velocities between the liquid and gas phases, the external flow is treated as a continuous gas phase, with dispersed liquid droplets. The velocities of the droplets are greatly influenced by the surrounding continuous phase because of their small mass. Due to drag forces, the droplets are, therefore, accelerated by the faster flowing gas phase. To determine the droplet drag force, the pressure and density of the surrounding gas must be known. It is necessary, therefore, to know the evaporation rate of the liquid and track the expansion of the spray cone. Using the measured experimental data, the effective spray droplet drag coefficient (C_D) is then determined at each location and is compared to data in existing literature from similar problems. Because of the similarity in exit flow parameters and measured spray characteristics among the nozzles, treatment assumptions and expressions are the same for all nozzle lengths considered in this study.

3.4.1. Representative droplet diameter distribution and evaporation rate

Theoretically, the evaporation rate of the liquid can be determined by tracking the change in droplet size distribution along the spray axis. Droplet sizes will reduce as liquid evaporates from the droplet surfaces. The PDPA, however, cannot measure accurately near the nozzle exit where the spray is very dense. Referring again to the droplet size measurements in Fig. 5b, there is not a trend of decreasing droplet size until after $z = 30$–40 mm. Since further away from the nozzle the PDPA measurements are reliable, the droplet sizes nearer to the nozzle can be determined by starting with the size measurement far from the nozzle, and back-calculating the droplet evaporation necessary for the measured temperature changes (Fig. 5c) through an energy and mass balance. The droplet diameter histograms measured at $z = 50$ mm for the 20 and 40 mm nozzles and at $z = 40$ mm for the 80 mm nozzle are fitted to a Gaussian distribution:

$$k(d) = \frac{1}{\sigma\sqrt{2\pi}} \exp\left(\frac{-(d-\bar{d})^2}{2\sigma^2}\right) \tag{6}$$

where σ is the standard deviation of the distribution and $\bar{d}$ is the mean value of diameter. The calculation is started at $z = 40$ mm for the 80 mm nozzle because that is the location of lowest temperature. Standard deviation is assumed to remain constant for each position.

The use of droplet size distributions is an improvement on a previous work by the authors [40] in which only a single representative droplet was used to account for the entire spray liquid volume. The latter over-predicted droplet sizes at the nozzle exit and overall droplet evaporation due to the much lower surface area to volume ratio of a single representative droplet in comparison to a droplet population.

The total distribution of droplet sizes, collectively, is taken to be the system of interest. The loss of internal energy of the population is equal to the latent heat of vaporization of the liquid (heating of droplets from the environment is assumed to be negligible relative to the latent heat of vaporization). The rate of evaporation is determined through a mass balance. The *Reynolds Transport Theorem* is used to determine the energy and mass balances of the droplet population:

$$-\frac{\partial}{\partial t}\int_{C_V} u\rho \mathrm{d}\forall = \int_{C_S} h_{fg}\rho\vec{v}\cdot\mathrm{d}\vec{A} \tag{7a}$$

$$-\frac{\partial}{\partial t}\int_{C_V} \rho \mathrm{d}\forall = \int_{C_S} \rho\vec{v}\cdot\mathrm{d}\vec{A} \tag{7b}$$

where h_{fg} is latent heat of vaporization. Liquid density is assumed to be constant and kinetic and potential energies are neglected in the energy equation. The reference internal energy is taken to be zero at $z = 40$–50 mm at the location of the start of the calculation, and internal energy change is calculated as $\Delta u = \Delta h = C\Delta T$, where C is the heat capacity of the liquid. Since fluid properties are taken to be constant, the volume and surface integrals of Eqs. (7a) and (7b) can be easily integrated:

$$-\frac{\partial}{\partial t} u\rho\forall = h_{fg}\rho v A \tag{8a}$$

$$-\frac{\partial}{\partial t} \rho\forall = \rho v A \tag{8b}$$

These equations are then combined and used to form a simple relation between the total droplet population volume between two points:

$$\forall_j\left(\frac{u_j - 2u_{j-1} + h_{fg}}{h_{fg} - u_{j-1}}\right) = \forall_{j-1} \tag{9}$$

where the time derivative is determined by simple differencing between two measurement points. To determine the total droplet volume, $\forall$, the following expression is used assuming all droplets are spheres:

$$\forall = \int_0^{d_{max}} \frac{4}{3}\pi\left(\frac{d}{2}\right)^3 \frac{1}{\sigma\sqrt{2\pi}} \exp\left(\frac{-(d-\bar{d})^2}{2\sigma^2}\right) dd \tag{10}$$

This equation is integrated from zero to the maximum expected diameter using the trapezoidal rule.

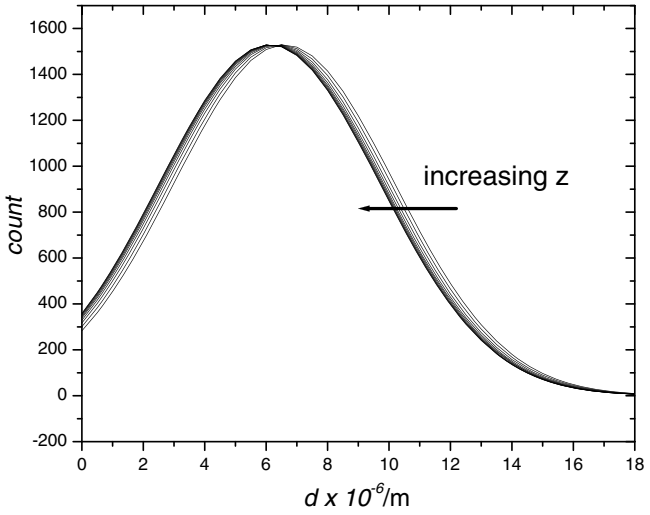

Fig. 7. Results of energy and mass balance on droplet diameter distribution.

The resulting droplet distributions for the 40-mm nozzle are plotted in Fig. 7 (distributions for the other two nozzles are similar so they are not shown). Note that these curves show a slight shift to the left with increasing z, indicating a gradual evaporation.

Next, vapor generation is determined by the difference in total droplet mass between measurement points multiplied by the total number of droplets existing at the nozzle exit:

$$G_j = [\rho_l(\forall_{j-1} - \forall_j)]\left[\frac{(1-\varepsilon_g)\left(\pi\frac{D^2}{4}\right)}{\int_0^{d_{max}} 4\pi\left(\frac{d_o}{2}\right)^2 \frac{1}{\sigma\sqrt{2\pi}}\exp\left(\frac{-(d_o-\bar{d}_o)^2}{2\sigma^2}\right)dd_o}\right] \tag{11}$$

where ε_g is void fraction at the nozzle exit. The first bracketed term represents the change in droplet mass due to evaporation while the second term is the theoretical number of droplets existing at the nozzle exit. The second term is estimated by the number of droplets necessary to occupy the liquid *area* at the exit. Eq. (11) can be used as a source term for vapor generation in spray modeling. For the present conditions, however, the effects of evaporation and vapor generation on gas phase densities are found to be very small since the majority of phase change appears to take place within the nozzle.

3.4.2. Spray cone gas pressure and density

Once the vapor generation has been calculated, the gas phase density and pressure evolution may be determined. First, the spray cone width as a function of z is measured from the high-speed flash lamp images of the spray. The measurement points are then fitted to a second-order exponential function to reduce measurement error as shown in Fig. 8a. Again, spray cone widths were similar for all three nozzle lengths so only the result for the 40 mm nozzle is shown.

Next, the gas phase pressures are solved by using a two-dimensional approach, considering slices of the spray cone at the measurement points, j (Fig. 8b). The gas properties are assumed to be uniform within each slice. The total mass of refrigerant gas at any point, M_{134a}, is determined by the sum of the mass of gas at the nozzle exit and the gas generated by evaporation, G. The ideal gas law with compressibility factor is then used to compute the partial pressure of the refrigerant gas:

$$p_{134a,j} = Z_{134a,j}\frac{M_{134a,j}R_{134a}T_j}{A_{g,j}L_j} \tag{12}$$

where Z is the compressibility factor at saturation conditions, A_g is total area of gas phase and L_j is the distance between j and $j-1$. A_g is determined by first calculating the area of the liquid and subtracting this from the total spray area determined from Fig. 8a.

$$A_{g,j} = A_{total,j} - A_{l,j} = A_{total,j} - \left(A_{l,j-1} - \frac{G_j}{\rho_l L_j}\right) \tag{13}$$

After exiting the nozzle, the calculated vapor pressure of the refrigerant appears to be below atmospheric pressure for all locations except for $z = 1$ mm, meaning the spray expands at a much faster rate than the rate of evaporation of liquid. The total gas pressure is, however, assumed to remain at least at atmospheric to avoid a vacuum condition. The remaining partial pressure necessary to reach atmospheric is assumed to come from dry air through entrainment. This allows for the calculation of total gas phase density, ρ_g, according to:

$$\rho_{g,j} = \frac{p_{134a,j}}{R_{134a}T_j} + \left(\frac{101,000 - p_{134a,j}}{R_{air}T_j}\right) \tag{14}$$

3.4.3. Droplet drag coefficients

After calculating the gas phase density, the drag coefficients relating the liquid and vapor phase velocities can be determined.

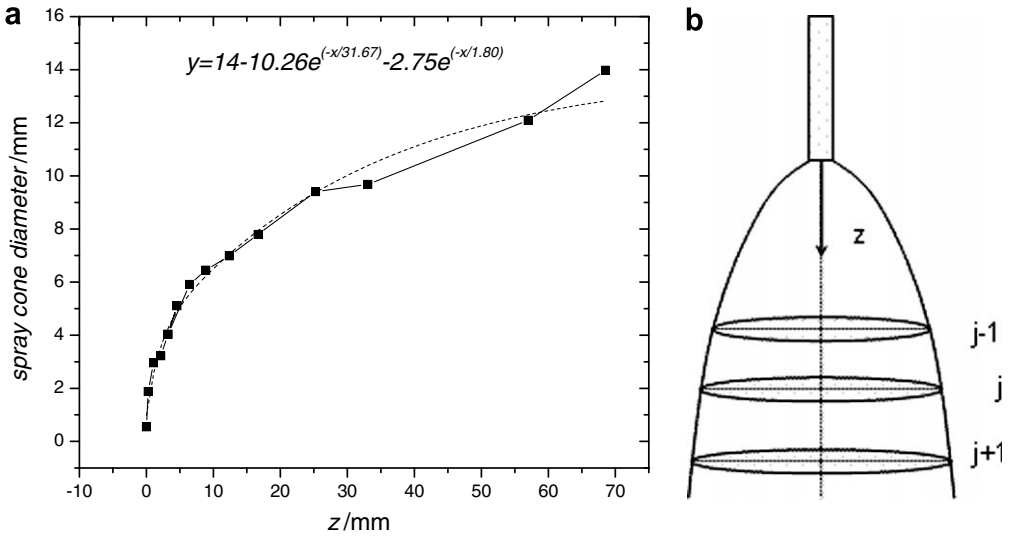

Fig. 8. (a) Spray cone diameter for 40 mm length nozzle and (b) 2-D slices of spray cone perpendicular to z at each measurement.

Unlike for droplet sizes, only *mean* droplet velocities need be considered because velocities are about the same for all droplet sizes, as verified by the diameter–velocity correlations determined from the PDPA measurements and shown in Fig. 9.

Using droplet velocity data, a drag force may be computed at each j location using Newton's Second Law.

$$F_D = \left(\rho_{l,j}\frac{4}{3}\pi r_j^3\right)\left(\frac{v_j - v_{j-1}}{t_j}\right) \quad (15)$$

where t_j is the time of flight of the droplet between j and $j-1$.

Drag force, however, can also be represented by the constitutive relation: $F_D = 0.5(v_g - v_l)^2 \rho C_D A$ where the term in parentheses is the *relative* velocity between the surrounding gas and droplet. This relation can be used to determine the drag coefficient between the liquid and gas phases:

$$C_D = \frac{2F_D}{\rho_g A (v_g - v_l)^2} \quad (16)$$

Computed drag coefficients for all nozzles are plotted together versus droplet *Re* in Fig. 10. The results exhibit an approximately linear relationship between C_D and *Re* so a least squares regression fit was performed and given below:

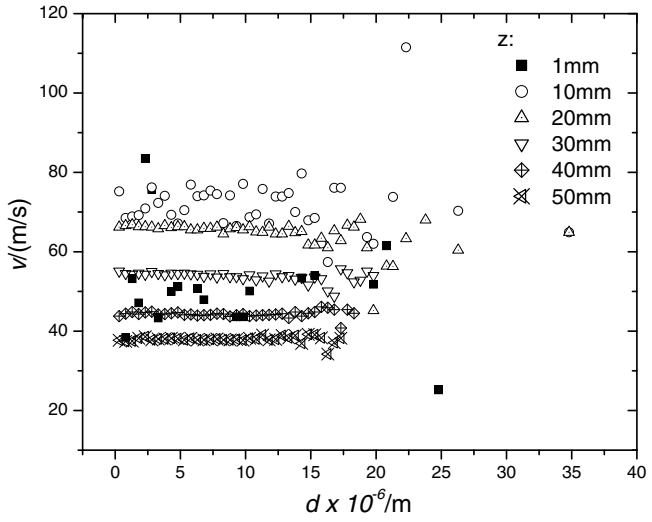

Fig. 9. Graph of droplet velocity versus diameter for the 40 mm length nozzle.

$$C_D = \frac{200}{Re^{1.6}} (0.1 < Re < 2000) \quad (17)$$

Some scatter is apparent in the higher *Re* range, from 20 to 2000, where droplets are very near the nozzle exit and velocity measurement errors are likely to be more significant. Within this *Re* range, the droplets may also be in a transition region where flow turbulence is a factor along with possible shockwave effects. The widely used Stokes and Kliachko drag relations [41] and Rudinger [42] relation are also shown for comparison. There is clear deviation from these relations, though the slope is nearly identical to Rudinger who obtained his expression using shock tube experiments. The Stokes relation also appears to approximate the current data well in the higher *Re* range but not in the low. The similarity in slope of Eq. (17) with the Rudinger correlation may be due to the fact that both were obtained under high accelerations. Flow perturbations are known to greatly influence drag coefficients and produce deviations from "classical" steady-state correlations. Also, droplet evaporation, which would clearly change liquid/gas interaction, may play a role. Future studies may help to clarify these and other effects, including treatment assumptions and measurement errors.

4. Conclusions

This work represents the first known effort quantifying internal nozzle flow parameters and its significance to the external spray characteristics of a flashing spray. It was found that for the conditions of high superheat and larger L/D ratio nozzles found in current dermatologic spray cooling devices, critical flow conditions are reached in which a choking condition develops at the nozzle exit. Increasing nozzle lengths had the effect of reducing liquid exit velocity and total mass flow rate while increasing the vaporization of the liquid phase and the gas phase velocity. External spray measurements, however, generally exhibited little difference among the nozzle lengths. This indicates that the differences in internal flow, namely the increased vaporization occurring in the longer nozzles, are not significant to the development of the resulting external flow. With nozzles of smaller aspect ratios, however, noticeable differences in external flow may occur and have indeed been observed by other researchers referenced earlier in the paper.

Spray droplet diameters were found to be unreliable within about 30 mm from the nozzle exit, but a technique was developed in which theoretical Gaussian droplet diameter distributions could be determined near the nozzle through mass and energy balances. Both liquid and gas phases were found to accelerate for some dis-

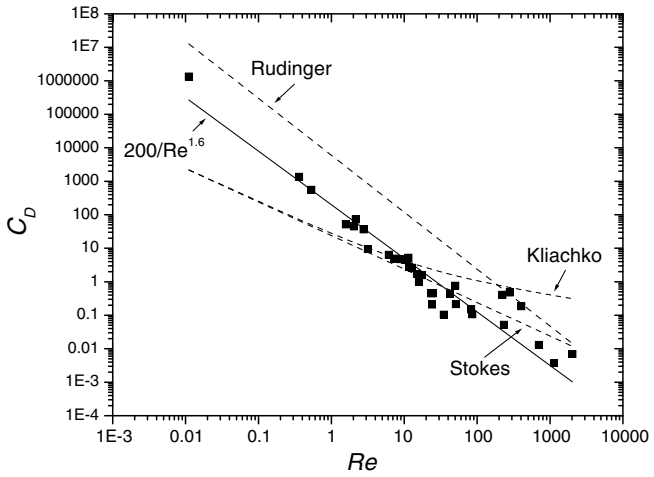

Stokes [41]	$\frac{24}{Re}$
Kliachko [41]	$\frac{24}{Re}\left(1+\frac{Re^{2/3}}{6}\right)$
Rudinger [42]	$\frac{6000}{Re^{1.7}}$ (50<*Re*<300)
Current Work	$\frac{200}{Re^{1.6}}$ (0.1<*Re*<2000)

Fig. 10. Flashing spray droplet drag coefficients and comparison to existing work.

tance away from the nozzle. Some new relations were also developed describing the interaction of the two phases and assumes that the droplets are suspended within the continuous gas phase and accelerated by its expansion. A new empirical correlation for C_D was developed for droplets under the higher acceleratory fields of flashing sprays. The results of this work may assist future modeling efforts of flashing spray formation and dispersion for many applications. For example, cryogen-assisted laser dermatology requires a strict control of the spray characteristics for maximal cooling efficiency and the fine tuning of cooling/heating sequences typical of short-duration spurts and laser pulses.

Acknowledgements

The authors would like to thank Wangcun Jia for technical assistance with PDPA operation; laboratory assistance provided by Kevin Chu, Joshua Yagoubian, and Alex Chaney; and Walfre Franco for helpful discussions. Funding was provided, in part, by the UC Riverside Academic Senate OMNIBUS grant.

Appendix

Because the gas phase pressure measurements are taken within a two-phase flow, the influence of the discontinuous liquid phase must be determined. The pressure induced by droplet impingement on the pressure transducer diaphragm may be determined by a simple momentum conservation:

$$p_d = \frac{F_d}{A_P} = \frac{\dot{m}_d v_d}{A_P} \tag{A.1}$$

where A_p is the area of the PDPA measurement probe (point of intersecting laser beams). In order to obtain the mass flow rate, the number of droplets passing through the probe must be determined. This is complicated by the fact that the number of valid droplet signals detected by the system does not necessarily represent the true number of droplets since undetected or invalidated droplets may exist. Others have considered this issue and developed statistical arguments to account for them. It is beyond the scope of this paper to describe them, so the reader is referred to an existing work [43].

The number flux of droplets passing through the pressure transducer extension tube was measured for the spray emitting from the 40 mm length nozzle. The extension tube was positioned 1 mm below the exit of the nozzle. Number flux was determined to be 68,000 l/s with an average droplet diameter and velocity of 9.6 μm and 13.8 m/s, respectively. Considering an approximate probe area of 5×10^{-8} m^2, the pressure induced by droplet impingement was found to be about 10 Pa. This value is insignificant compared to the precision level of the pressure transducer used.

References

[1] J.S. Nelson, T.E. Milner, B. Anvari, B.S. Tanenbaum, S. Kimel, L.O. Svaasand, S.L. Jacques, Dynamic epidermal cooling during pulsed-laser treatment of port-wine stain – a new methodology with preliminary clinical-evaluation, Arch. Dermatol. 131 (1995) 695–700.
[2] C.J. Chang, J.S. Nelson, Cryogen spray cooling and higher fluence pulsed dye laser treatment improve port-wine stain clearance while minimizing epidermal damage, Dermatol. Surg. 25 (1999) 767–772.
[3] W. Franco, J. Liu, R. Romero-Mendez, W.C. Jia, J.S. Nelson, G. Aguilar, Extent of lateral epidermal protection afforded by a cryogen spray against laser irradiation, Laser Surg. Med. 39 (2007) 414–421.
[4] T.J. Pfefer, D.J. Smithies, T.E. Milner, M.J.C. van Gemert, J.S. Nelson, A.J. Welch, Bioheat transfer analysis of cryogen spray cooling during laser treatment of port wine stains, Laser Surg. Med. 26 (2000) 145–157.
[5] J.W. Tunnell, L.V. Wang, B. Anvari, Optimum pulse duration and radiant exposure for vascular laser therapy of dark port-wine skin: a theoretical study, Appl. Opt. 42 (2003) 1367–1378.
[6] W. Verkruysse, B. Majaron, B.S. Tanenbaum, J.S. Nelson, Optimal cryogen spray cooling parameters for pulsed laser treatment of port wine stains, Laser Surg. Med. 27 (2000) 165–170.
[7] B.M. Pikkula, J.H. Torres, J.W. Tunnell, B. Anvari, Cryogen spray cooling: effects of droplet size and spray density on heat removal, Laser Surg. Med. 28 (2001) 103–112.
[8] G. Aguilar, G.X. Wang, J.S. Nelson, Dynamic behavior of cryogen spray cooling: effects of spurt duration and spray distance, Laser Surg. Med. 32 (2003) 152–159.
[9] S.S. Hsieh, H.H. Tsai, Thermal and flow measurements of continuous cryogenic spray cooling, Arch. Dermatol. Res. 298 (2006) 82–95.
[10] R. Brown, J.L. York, Sprays formed by flashing liquid jets, AIChE J. 8 (1962) 149–153.
[11] R.D. Reitz, A photographic study of flash-boiling atomization, Aerosol Sci. Technol. 12 (1990) 561–569.
[12] B.S. Park, S.Y. Lee, An experimental investigation of the flash atomization mechanism, Atom. Spray 4 (1994) 159–179.
[13] E.M. Peter, A. Takimoto, Y. Hayashi, Flashing and shattering phenomena of superheated liquid jets, JSME Int. J. Ser. B-Fluid Therm. Eng. 37 (1994) 313–321.
[14] J.T. Allen, Laser-based measurements in two-phase flashing propane jets. Part I: velocity profiles, J. Loss Prevent. Process Ind. 11 (1998) 291–297.
[15] J.T. Allen, Laser-based measurements in two-phase flashing propane jets. Part II: droplet size distribution, J. Loss Prevent. Process Ind. 11 (1998) 299–306.
[16] E. Sher, C. Elata, Spray formation from pressure cans by flashing, Ind. Eng. Chem. Process Des. Develop. 16 (1977) 237–242.
[17] Y.B. Zeng, C.F.F. Lee, An atomization model for flash boiling sprays, Combust. Sci. Technol. 169 (2001) 45–67.
[18] D. Yildiz, P. Rambaud, J. Van Beeck, J.M. Buchlin, Evolution of the spray characteristics in superheated liquid jet atomization in function of initial flow conditions, in: 10th International Conference on Liquid Atomization and Spray Systems, Kyoto, Japan, 2006, ICLASS06-122.
[19] E. Hervieu, T. Veneau, Experimental determination of the droplet size and velocity distributions at the exit of the bottom discharge pipe of a liquefied propane storage tank during a sudden blowdown, J. Loss Prevent. Process Ind. 9 (1966) 413–425.
[20] J. Senda, M. Yamaguchi, T. Tsukamoto, H. Fujimoto, Characteristics of spray injected from gasoline injector, JSME Int. J. Ser. B-Fluid Therm. Eng. 37 (1994) 931–936.
[21] G. Knubben, C.W.M. van der Geld, Drop size distribution evolution after continuous or intermittent injection of butane or propane in a confined air flow, Appl. Therm. Eng. 21 (2001) 787–811.
[22] Y. Nishimura, Y. Wada, A. Yamaguchi, J.K. Yoon, J. Senda, H. Fujimoto, An experimental study on flash boiling spray using two-component fuel under the condition of advanced injection HCCI, in: 10th International Conference on Liquid Atomization and Spray Systems, Kyoto, Japan, 2006, ICLASS06-134.
[23] S. Lin, C.C.K. Kwok, R.Y. Li, Z.H. Chen, Z.Y. Chen, Local frictional pressure-drop during vaporization of R-12 through capillary tubes, Int. J. Multiphase Flow 17 (1991) 95–102.
[24] F. Escanes, C.D. Perez-Segarra, A. Oliva, Numerical-simulation of capillary-tube expansion devices, Int. J. Refrigerat. – Rev. Int. Du Froid 18 (1995) 113–122.
[25] O. García-Valladares, Review of numerical simulation of capillary tube using refrigerant mixtures, Appl. Therm. Eng. 24 (2004) 949–966.
[26] Reference Fluid Thermodynamic and Transport Properties Database (REFPROP), 7.0 ed. Gaithersburg, MD: National Institute of Standards and Technology, 2002.
[27] S.Z. Rouhani, E. Axelsson, Calculation of void volume fraction in subcooled and quality boiling regions, Int. J. Heat Mass Transfer 13 (1970) 383–393.
[28] S.W. Churchill, Friction-factor equation spans all fluid-flow regimes, Chem. Eng. 84 (1977) 91–92.
[29] L. Friedel, Improved friction pressure drop correlation for horizontal and vertical two-phase pipe flow, in: European Two-Phase Flow Group Meeting, Ispra, Italy, 1979, paper E2.
[30] M.M. Shah, Chart correlation for saturated boiling heat transfer: equations and further study, ASHRAE Trans. 88 (1982) 185–196.
[31] S.W. Churchill, H.H.S. Chu, Correlating equations for laminar and turbulent free convection from a vertical plate, Int. J. Heat Mass Transfer 18 (1975) 1323–1329.
[32] O. García-Valladares, Numerical simulation of non-adiabatic capillary tubes considering metastable region. Part I: Mathematical formulation and numerical model, Int. J. Refrigerat. – Rev. Int. Du Froid 30 (2007) 642–653.
[33] W.D. Bachalo, Experimental methods in multiphase flows, Int. J. Multiphase Flow 20 (1994) 261–295.
[34] W.D. Bachalo, The phase doppler method – analysis, performance evaluations, and applications, Particle Particle Syst. Charact. 11 (1994) 73–83.
[35] D. Yildiz, J. van Beeck, M.L. Riethmuller, Feasibility exploration of laser-based techniques for characterization of a flashing jet, Particle Particle Syst. Charact. 21 (2004) 390–402.
[36] J.T. Allen, R.J. Bettis, Valid data abstraction from LDA measurements in two-phase propane releases, in: Proceedings of the Seventh International Conference on Laser Anemometry-Advances and Applications, Karlsruhe, Germany, 1997, pp. 509–516.
[37] W.D. Bachalo, Laser Doppler velocimetry primer NASA CR 177386, Nat. Aeronaut. Space Admin. (1985).
[38] R.W. Tate, Some problems associated with the accurate representation of droplet size distributions, in: Proceedings of the Second International Conference on Liquid Atomization and Spray, 1982, pp. 341–351.

[39] G. Aguilar, B. Majaron, W. Verkruysse, Y. Zhou, J.S. Nelson, E.J. Lavernia, Theoretical and experimental analysis of droplet diameter, temperature, and evaporation rate evolution in cryogenic sprays, Int. J. Heat Mass Transfer 44 (2001) 3201–3211.
[40] H. Vu, O. García-Valladares, G. Aguilar, Insights into flashing spray characteristics using a capillary tube expansion model, in: 20th Annual ILASS-Americas Conference, Chicago, IL, 2007, paper 091.
[41] N.A. Fuchs, The Mechanics of Aerosols, Revised and Enlarged ed., Macmillan, New York, 1964.
[42] G. Rudinger, Effective drag coefficient for gas-particle flow in shock tubes, J. Basic Eng. 92 (1970) 165–172.
[43] I.V. Roisman, C. Tropea, Flux measurements in sprays using phase Doppler techniques, Atom. Spray 11 (2001) 667–699.